



Driving Waveform Optimization by Simulation and Numerical Analysis for Suppressing Oil-Splitting in Electrowetting Displays

Shufa Lai¹, Qinghua Zhong^{2*} and Hailing Sun¹

¹Guangdong Provincial Key Laboratory of Optical Information Materials and Technology and Institute of Electronic Paper Displays, South China Academy of Advanced Optoelectronics, South China Normal University, Guangzhou, China, ²School of Physics and Telecommunication Engineering, South China Normal University, Guangzhou, China

OPEN ACCESS

Edited by:

Feng Chi,
University of Electronic Science and
Technology of China, China

Reviewed by:

Jiasheng Li,
South China University of Technology,
China
Xiaowen Zhang,
Guilin University of Electronic
Technology, China

*Correspondence:

Qinghua Zhong
zhongqinghua@m.scnu.edu.cn

Specialty section:

This article was submitted to
Optics and Photonics,
a section of the journal
Frontiers in Physics

Received: 04 June 2021

Accepted: 02 July 2021

Published: 15 July 2021

Citation:

Lai S, Zhong Q and Sun H (2021)
Driving Waveform Optimization by
Simulation and Numerical Analysis for
Suppressing Oil-Splitting in
Electrowetting Displays.
Front. Phys. 9:720515.
doi: 10.3389/fphy.2021.720515

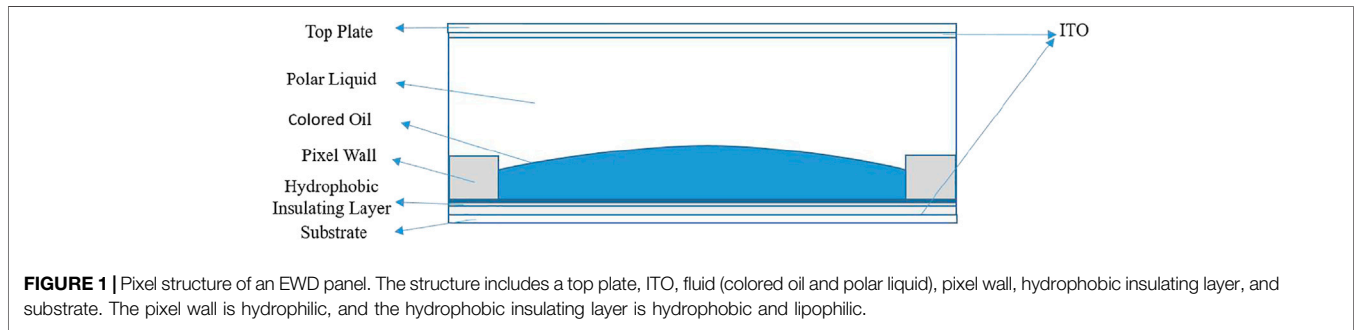
Electrowetting display (EWD) is a new reflective display device with low power consumption and fast response speed. However, the maximum aperture ratio of EWDs is confined by oil-splitting. In order to suppress oil-splitting, a two-dimensional EWD model with a switch-on and a switch-off process was established in this paper. The process of oil-splitting was obtained by applying different voltage values in this model. Then, the relationship between the oil-splitting process and the waveforms with different slopes was analyzed. Based on this relationship, a driving waveform with a narrow falling ramp, low-voltage maintenance, and a rising ramp was proposed on the basis of square waveform. The proposed narrow falling ramp drove the oil to rupture on one side. The low-voltage maintenance stage drove the oil to shrink with a whole block. The proposed rising ramp was pushed the oil into a corner quickly. The experimental results showed that the oil splitting can be suppressed effectively by applying the proposed driving waveform. The aperture ratio of the proposed driving waveform was 2.9% higher than that of the square waveform with the same voltage.

Keywords: driving waveform, electrowetting display, oil-splitting, modeling and simulation, oil movement

INTRODUCTION

Electrowetting (EW) is a phenomenon which can change the wettability of solid-liquid surface by using electric field [1]. The theory of EW was first proposed in 1981 [2]. In recent years, EW technology has been widely used in the chemical industry, bioengineering, display, and other fields [3–5]. Among them, the EWD is a new reflective display technology after electrophoretic display technology [6, 7]. Compared with conventional display technologies [8, 9], the EWD technology has the advantages of low power consumption, high contrast, fast response, and full color [10, 11], which is considered one of the most attractive emerging display technologies [12].

An EWD pixel is mainly composed of substrate, ITO (Indium Tin Oxides) guide electrode, hydrophobic insulation layer, pixel wall, colored oil, polar liquid, and top plate as shown in **Figure 1** [13, 14]. A complete driving process of EWD can be divided into two stages. In the first stage, a suitable voltage is applied between upper and lower electrodes, the colored oil is pushed into a corner. The color of bottom substrate is displayed in pixels. When the voltage is removed, the hydrophobic layer is completely covered by the colored oil again. The color of colored oil is displayed in pixels [15].



At present, there are still some defects in EWDs, such as oil-splitting, charge trapping, oil overflow, and so on [10]. To solve these defects and further improve the display performance of EWDs, many researchers have made many attempts. For example, a three-dimensional EWD model was established and the process of fluid flow was simulated. In the simulation, the principle of phase-field was used to simulate the movement of oil interface successfully, and the influence of contact angle of the pixel wall on oil-splitting was studied [16]. However, the problem of oil-splitting caused by high voltage had not been solved. For oil-splitting, the influence of surface tension and contact angle in the fluid was considered. Through model simulation and numerical analysis, the influence of contact angle and surface tension on oil-splitting was proved [17]. In addition, the oil-splitting was affected by the oil thickness. The oil in the EWDs pixel was non-uniform, and the oil was split at the thinnest point [18]. However, the influence of thickness change on the process of oil movement was not considered. To suppress the oil-splitting, a driving waveform which consisted of four stages: starting, rising, displaying, and recovering was proposed. Starting from a low voltage to drive the oil can suppress oil-splitting effectively [19]. However, the speed of oil movement was slowed down.

In order to suppress the oil-splitting, a simulation model was established by COMSOL Multiphysics software. The relationship between electrostatic field force and oil shape change was studied by this model. And then, the change characteristic of oil shape was obtained in a switch-on process. According to this characteristic, a driving waveform which can suppress the oil-splitting effectively was proposed.

NUMERICAL METHODOLOGY

The simulation of EWDs was implemented by establishing and calculating numerical equations. It was done to track the change of the oil-water interface in the model [20]. By using COMSOL Multiphysics software and Finite-Element method to simulate Two-Phase laminar flow with the electrostatic field, the physical field of laminar flow was coupled with the phase-field and the electrostatic field [21]. The finite element analysis method can be used to solve numerical calculation problems including the Cahn-Hilliard equation, Laplace equation, and Navier-Stokes equation

[22]. Meanwhile, to solve Maxwell's stress tensor equation, an electrostatic field module was added to the simulation. The electrostatic field force of the electrostatic field module was fed back into the laminar flow module. The Navier-Stokes equation and phase-field equation were solved according to specified boundary conditions and calculation results of electrostatic field.

Governing Equations

Phase-field is used to describe the dynamic process of a two-phase flow interface. The movement of interface is tracked indirectly by solving two equations. One of them is used to solve phase-field variable \varnothing and the other is used to solve the mixed energy density ψ [16, 23, 24]. The position of the interface is determined by minimum free energy [23]. A large number of data have been proved that the phase-field method could effectively predict droplet movement on the solid surface [25, 26]. **Eqs. 1–3** represent the governing equation of phase-field [27]. **Eq. 4** describes the relationship between γ and ε .

$$\frac{\partial \varnothing}{\partial t} + u \cdot \nabla \varnothing = \nabla \cdot \frac{\gamma \lambda}{\varepsilon^2} \nabla \psi \quad (1)$$

$$\psi = -\nabla \cdot \varepsilon^2 \nabla \varnothing + (\varnothing^2 - 1) \varnothing + \left(\frac{\varepsilon^2}{\lambda} \right) \frac{\partial f_{ext}}{\partial \varnothing} \quad (2)$$

$$\sigma = \frac{2\sqrt{2}}{3} \frac{\lambda}{\varepsilon} \quad (3)$$

$$\gamma = \chi \varepsilon^2 \quad (4)$$

Where λ is the energy density and ε is the capillary width. **Eq. 3** describes the relationship between these two parameters and the surface tension coefficient σ . The γ is the mobility parameter and χ is the mobility tuning parameter in **Eq. 4**. \varnothing was set to 1 for oil and -1 for water. In order to couple the electrostatic field with the laminar flow field, the dielectric constant, density, and viscosity between diffusion interfaces need to be calculated by **Eqs. 5–7**.

$$\rho = \rho_1 + (\rho_2 - \rho_1) \varnothing \quad (5)$$

$$\mu = \mu_1 + (\mu_2 - \mu_1) \varnothing \quad (6)$$

$$\varepsilon_r = \varepsilon_{r1} + (\varepsilon_{r2} - \varepsilon_{r1}) \varnothing \quad (7)$$

Where ρ , μ , and ε_r represent the density, viscosity, and dielectric constant of fluids, respectively. The mean curvature between the two liquids interfaces was calculated by **Eqs. 8,9** [27].

$$\kappa = 2(1 + \varnothing)(1 - \varnothing) \frac{G}{\sigma} \quad (8)$$

$$G = \lambda \left(-\nabla^2 \varnothing + \frac{\varnothing(\varnothing^2 - 1)}{\varepsilon^2} \right) + \frac{\partial f}{\partial \varnothing} \quad (9)$$

Where κ and G represent the mean curvature and the chemical potential, respectively.

The laminar flow field can be solved by the Navier-Stokes equation and continuity equation [28]. The Navier-Stokes equation is described as **Eq. 10**. To depict the movement of two immiscible liquids, the transport of mass and momentum are governed by incompressible Navier–Stokes equations.

$$\rho \left(\frac{\partial u}{\partial t} + u \cdot \nabla u \right) = -\nabla p + \nabla \cdot \left(\mu (\nabla u + (\nabla u)^T) - \frac{2}{3} u (\nabla \cdot u) I \right) + F \quad (10)$$

$$F = F_{st} + \rho g + F_{vf} \quad (11)$$

Where u , p , ρ , and μ represent the velocity, pressure, density, and dynamic viscosity of the fluid respectively. Each term in **Eq. 10** corresponds to the inertial force, pressure, viscous force, and external force, respectively. The external force consists of surface tension, gravity, and a volume force, the F_{st} , g and F_{vf} represent the surface tension, gravity acceleration, and volume force, respectively.

As stated in **Eqs. 10, 11**, the coupling between the laminar flow field and the electrostatic field is achieved by applying the electrostatic volume force to the Navier-Stokes equation. The electrostatic field force is the main factor that can cause fluid-flowing [16]. In addition, the electrostatic field force can be obtained by calculating the divergence based on Maxwell Stress Tensor (MST) [16], and the calculation is expressed in **Eq. 12**.

$$F_{vf} = \nabla T_{ik} \quad (12)$$

MST formula is described by **Eq. 13**.

$$T = ED^T - \frac{1}{2} (D \cdot EI) \quad (13)$$

Where I is the identity matrix, E is the electric field and D is the electric displacement field, and their relationship is described by **Eqs. 14, 15**.

$$E = -\nabla V \quad (14)$$

$$D = \varepsilon_0 \varepsilon_r E \quad (15)$$

In a two-dimensional model simulation, the MST is expressed as **Eq. 16**.

$$T = \begin{bmatrix} T_{xx} & T_{xy} \\ T_{yx} & T_{yy} \end{bmatrix} \quad (16)$$

Eq. 17 can be obtained by substituting parameters.

$$T = \begin{bmatrix} \varepsilon_0 \varepsilon_r E_x^2 - \frac{1}{2} \varepsilon_0 \varepsilon_r (E_x^2 + E_y^2) & \varepsilon_0 \varepsilon_r E_x E_y \\ \varepsilon_0 \varepsilon_r E_x E_y & \varepsilon_0 \varepsilon_r E_y^2 - \frac{1}{2} \varepsilon_0 \varepsilon_r (E_x^2 + E_y^2) \end{bmatrix} \quad (17)$$

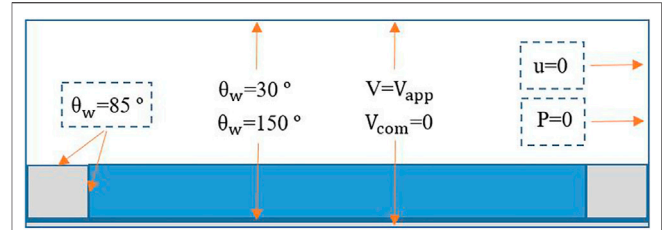


FIGURE 2 | The boundary conditions for the electrostatic field, phase field, and laminar flow field. Where u , P , θ_w , and V represents the velocity, pressure, contact angle, and voltage of the boundary conditions respectively. The pixel wall and outlet are symmetrical boundary conditions.

Where E_x and E_y represent the horizontal and vertical electric fields respectively. The variation of volume force caused by the electrostatic field acts on the interface between oil and water, and the calculation can be expressed in **Eq. 18**.

$$F = \begin{bmatrix} \frac{\partial(T_{xx})}{\partial x} & \frac{\partial(T_{xy})}{\partial y} \\ \frac{\partial(T_{yx})}{\partial x} & \frac{\partial(T_{yy})}{\partial y} \end{bmatrix} \quad (18)$$

When an electric field is applied, the water is in contact with the hydrophobic insulation layer with the action of electrostatic field force [29, 30], the electrostatic field force can be described by **Eq. 19**.

$$F_e = \frac{1}{2} d_{hyd} \varepsilon_0 \varepsilon_{hyd} E_{hyd}^2 \quad (19)$$

Where d_{hyd} , ε_{hyd} and E_{hyd} represent the thickness of the hydrophobic insulation layer, dielectric constant, and electric field strength on the hydrophobic insulation layer, respectively. Therefore, the force balance on the contact line can be derived from the Lippmann-Young equation, as shown in **Eq. 20**.

$$\cos \theta_e = \cos \theta_{hyd} + \frac{\varepsilon_0 \varepsilon_{hyd} V^2}{2 d_{hyd} \gamma_{ow}} \quad (20)$$

Where θ_e , θ_{hyd} , and γ_{ow} are the EW contact angle, Young's contact angle of the hydrophobic dielectric layer, and the surface tension, respectively.

Boundary Conditions

In the simulation model, boundary conditions are the prerequisites for determining the solution of governing equations on the boundary. The zero-charge boundary condition should be set on all sides of the model. For electrostatic field boundary conditions, the voltage V and the ground need to be specified. The wetted wall, the initial interface, and the outlet need to be specified in phase-field boundary conditions. The wetted wall boundary can be calculated by **Eqs. 21, 22**.

$$n \cdot \varepsilon^2 \nabla \varnothing = \varepsilon^2 \cos(\theta_w) |\nabla \varnothing| \quad (21)$$

TABLE 1 | Structure, material, and interface parameters of the model.

Parameters	Quantity	Symbol	Value	Unit
Material	Density of oil	ρ_{oil}	800	kg/m ³
	Density of water	ρ_{water}	1,000	kg/m ³
	Dynamic viscosity of oil	μ_{oil}	0.0005–0.003	Pa·s
	Dynamic viscosity of water	μ_{water}	0.001	Pa·s
	Dielectric constant of oil	ϵ_{oil}	2.8	1
	Dielectric constant of water	ϵ_{water}	88	1
	Dielectric constant of a hydrophobic dielectric layer	ϵ_{hyd}	1.6	1
Structure	Dielectric constant of a grid	ϵ_{grid}	3.6	1
	Width of a pixel	W_{pixel}	160	μm
	Height of a grid	d_{grid}	6	μm
	Width of a grid	W_{grid}	15	μm
	Thickness of a hydrophobic dielectric layer	d_{hyd}	1	μm
	Thickness of oil	d_{oil}	6	μm
	Interfacial	Surface tension of oil and water	γ_{ow}	0.02
Contact angle of a grid		θ_{grid}	85	deg
Contact angle of a hydrophobic insulating layer		θ_{hyd}	150	deg
Contact angle of the top plate		θ_{top}	30	deg

$$n \cdot \frac{\gamma\lambda}{\epsilon^2} \nabla\psi = 0 \quad (22)$$

The interface of the two-phase flow was selected as an initial boundary condition. Both sides of the model (except the pixel walls) were selected as inlet and outlet boundary conditions. In addition, initial values of pressure and velocity in the laminar flow field were set to 0. The wall condition was set to no slip. These setting of boundary conditions were shown in **Figure 2**. The dotted box in **Figure 2** represents the symmetric boundary condition.

PROCESS AND DISCUSSION

The parameters used in the simulation were shown in **Table 1**. The fluid (oil and water) in the model was set to incompressible flow. It was assumed that the temperature (25°C) was kept constant during the fluid movement, so the thermal expansion of the fluid was ignored. The influence of pressure on dynamic viscosity was ignored. In addition, the Bond number describes the relationship between gravity and surface tension in the EWDs model, and it is far less than 1. So the gravity can be neglected [16]. In the simulation, the polar liquids were replaced by water [31].

The proposed simulation model was shown in **Figure 2**. The natural spreading and shrinking process of oil were realized in this model. To describe the display performance of EWDs, it is necessary to calculate the aperture ratio. The aperture ratio is an important performance index of EWDs, which is a proportion of opening area in a whole pixel [20]. When the aperture ratio was calculated in two dimensions, the bottom of the EWD was considered as a square, and A_r is used to represent the aperture ratio, L is the length of the contact line between the oil and the hydrophobic insulating layer in two dimensions structure, and d is the area of the hydrophobic insulating layer. The aperture ratio was calculated by using **Eq. 23**.

$$A_r = \frac{4 \times d^2 - \pi L^2}{4 \times d^2} \times 100\% \quad (23)$$

When the electric field inside a pixel was analyzed, the electric field formula was used, as shown in **Eq. 24**. Where E , U , d represents the electric field, the voltage, and the distance between the two potentials, respectively.

$$E = \frac{U}{d} \quad (24)$$

In this paper, the EWD model was implemented by COMSOL Multiphysics 5.4. The aperture ratio test platform was shown in **Figure 3**. This test platform included a waveform editing system, a signal amplifier, and a detection system. The waveform editing system was used to edit and generate waveform signals, which was consisted of a computer and a function signal generator. The signal was amplified by the signal amplifier to drive the oil. The detection system was used to collect oil movement image of EWD panel in real time, which was consisted of a high-speed camera and an image processing system. The aperture ratio was obtained by the image processing platform.

Influence of Dynamic Viscosity

The dynamic viscosity is an important parameter in fluid. The dynamic viscosity of oil can affect the aperture ratio and response time [20]. The response time is expressed as T . In one driving cycle, the time for applying the driving waveform is represented by T_1 , and the time when the pixel reaches the maximum aperture ratio is represented by T_2 . The response time is equal to the difference between T_2 and T_1 . In this paper, an experiment of oil dynamic viscosity from 0.0005 Pa·s to 0.003 Pa·s with an interval of 0.0005 Pa·s was designed, and the experimental results were shown in **Figure 4**. When the dynamic viscosity was changed from 0.002 Pa·s to 0.003 Pa·s, the response time was shorter and the aperture ratio was larger. **Figure 5** showed that when the dynamic viscosity of oil was less than 0.0015 Pa·s, the oil was split into two pieces. Otherwise, the oil was pushed into a

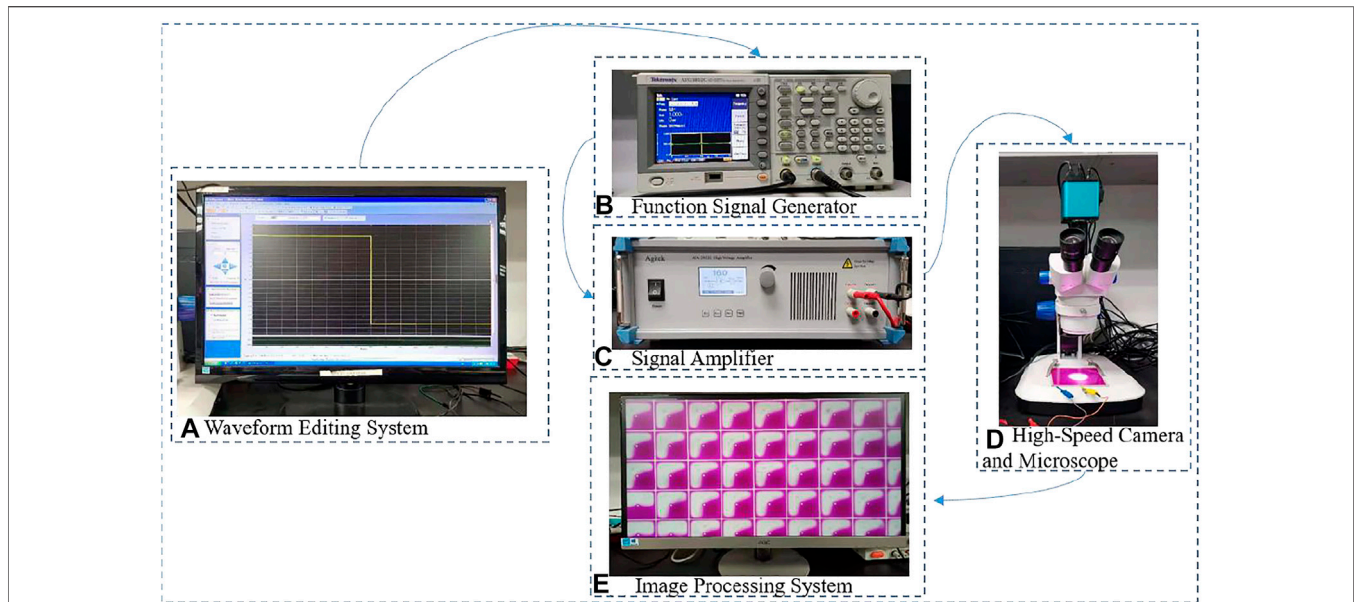


FIGURE 3 | An aperture ratio test platform for EWDs (A) A waveform editing system (B) A function signal generator (C) A signal amplifier (D) A high-speed camera and a microscope (E) An image processing system.

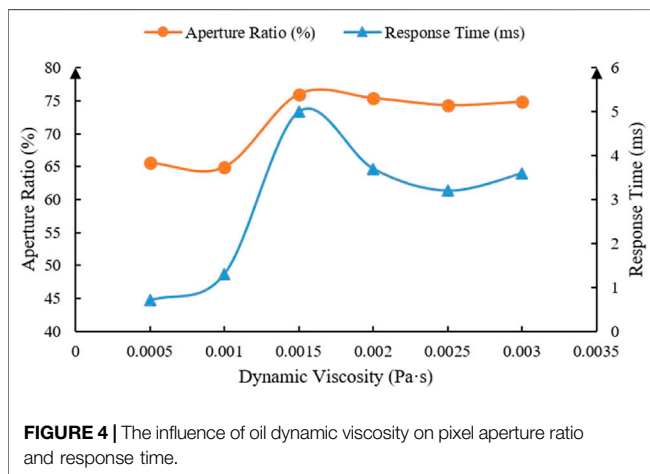


FIGURE 4 | The influence of oil dynamic viscosity on pixel aperture ratio and response time.

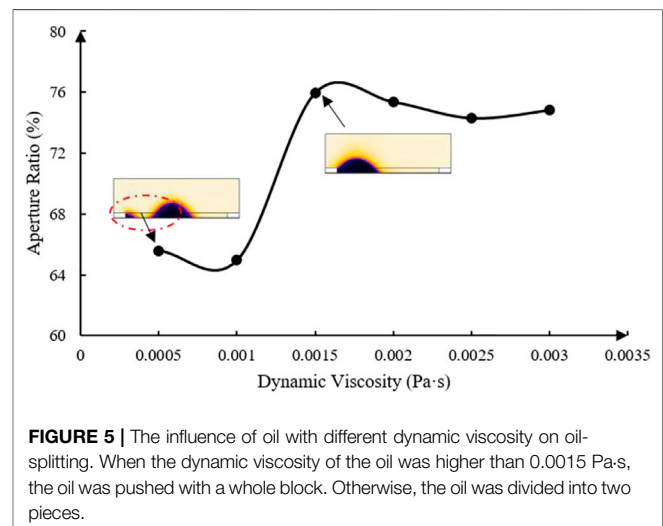


FIGURE 5 | The influence of oil with different dynamic viscosity on oil-splitting. When the dynamic viscosity of the oil was higher than 0.0015 Pa·s, the oil was pushed with a whole block. Otherwise, the oil was divided into two pieces.

corner with a whole block. Therefore, the oil with a dynamic viscosity from 0.002 Pa·s to 0.003 Pa·s should be selected in current conditions. **Figure 6** showed the process of a switch-on and a switch-off in a pixel with specific conditions. The conditions were that the voltage was 32 V and the oil dynamic viscosity was 0.002 Pa·s. The results showed that the oil was pushed into a corner with a whole block. So, the dynamic viscosity of oil was set to 0.002 Pa·s.

Influence of Driving Waveforms

In a pixel, the voltage of driving waveform was converted into electrostatic field force and applied to the water and oil. In the simulation, the gradually increasing voltage was set by the parametric scanning method, and the results were shown in **Figure 7**. When the voltage was lower than 16 V, the shape of oil was squeezed down at both sides of a pixel, but the oil was not

split. When the voltage was changed from 16 to 36 V, the aperture ratio was almost increased linearly. When the voltage was higher than 36 V, the aperture ratio was increased slowly and reached the maximum. At the same time, the oil was split into two pieces. The blue curve in **Figure 7** represented the maximum aperture ratio of an actual EWD pixel when the voltage was changed from 16 to 36 V. The length and width of an actual pixel were 150 and 150 μm , respectively. The aperture ratio of the actual pixel was measured on the test platform in **Figure 3**. The results showed that the value of simulation was close to the actual before 20 V. In the range of 20–28 V, the simulation value was 4.3% higher than the actual, and in the range of 28–36 V, the simulation value was 10.5% higher than the actual. Altogether, the trends between

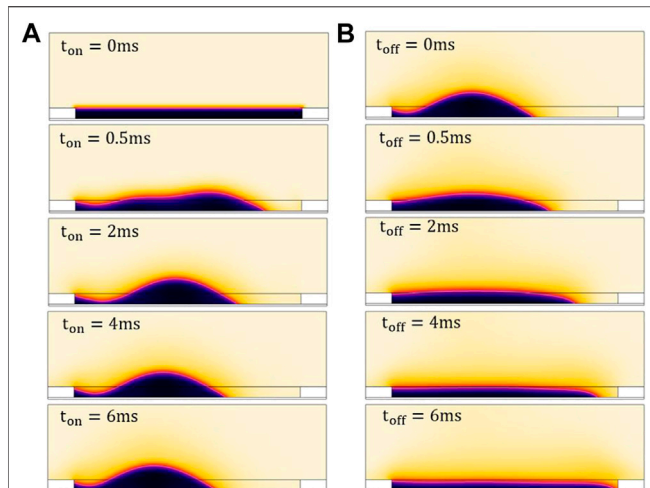


FIGURE 6 | In COMSOL software, the movement process of oil and water (black represents oil, light yellow represents water) was intercepted **(A)** After applying 32 V voltage, the oil was shrunk with the action of electrostatic field force, which was completed in 4 ms. **(B)** When the driving voltage was removed, the oil was naturally spread, and the process was completed in 6 ms.

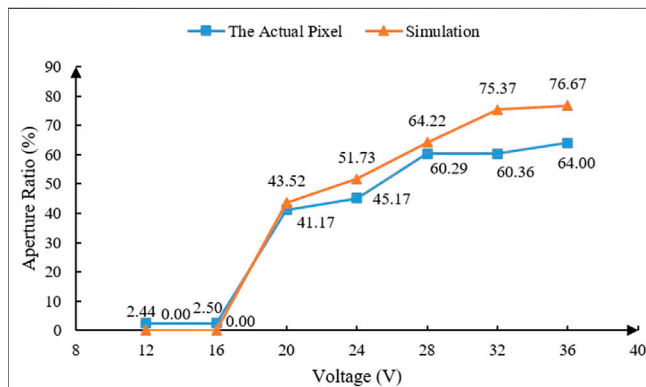


FIGURE 7 | The aperture ratio between simulation and an actual pixel. When the voltage was changed from 16 to 36 V, the change curve of aperture ratio between the actual pixel and simulation was obtained. The length and width of an actual pixel were 150 and 150 μm respectively. The changing trend of aperture ratio was consistent between simulation and actual EWD pixel.

these two were consistent. Therefore, the accuracy of this simulation model was verified.

The driving waveform has influence on the movement of oil [32–34]. To comprehend the acceleration ability of oil with the action of driving waveforms in one cycle, these driving waveforms with a different rising slope were designed, as shown in **Figure 8**. The change of aperture ratio with the action of four driving waveforms was shown in **Figure 9**. With the slope increased, the response time was shorter. When the slope was infinite (square waveform), the oil was split into two pieces. The experimental data showed that the moment when the pixel reached the maximum aperture ratio later

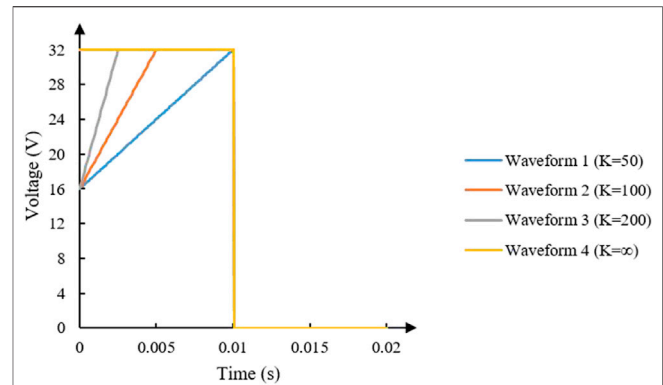


FIGURE 8 | Four driving waveforms with different slopes were designed. The starting voltage was set to 16 V. K in the left was the slope, and the slopes of the four waveforms are 50, 100, 200, and infinite, respectively. The effective driving cycle was 10 ms, and the latter 10 ms was set to 0 V.

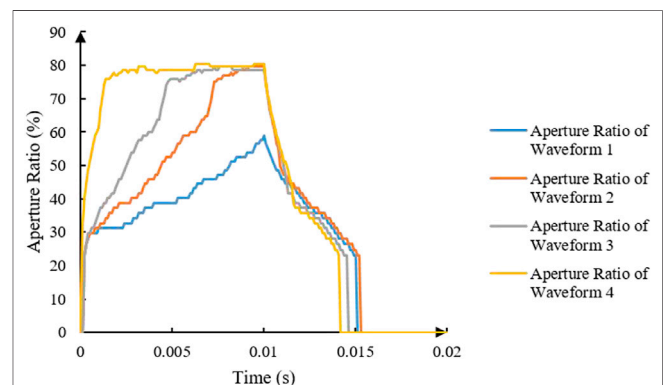


FIGURE 9 | The pixel aperture ratio was obtained with four driving waveforms.

than the moment that the driving waveform reached the maximum voltage for 2–5 ms. The greater the slope, the stronger the oil acceleration. So, a maintenance period of 2–5 ms should be set to drive a pixel for reaching the maximum aperture ratio. It took more than 6 ms in the natural spreading stage.

Relationship Between Electrostatic Field Force and Oil Movement

The forces on the fluid can be divided into volume force and external force. The volume force can be divided into surface tension and electrostatic field force. The electrostatic field force is a key factor that affects the oil movement of EWDs [35, 36]. To obtain the relationship between the movement status of oil with a whole block and the internal electrostatic field force. Parameters were determined based on Waveform 2 in **Figure 8**, the voltage was set to 32 V and the oil dynamic viscosity was 0.002 Pa·s.

The change of the internal electric field inside a pixel was shown in **Figure 10**. In the vertical direction, the internal space of the pixel was divided into a water channel and an oil-water mixed

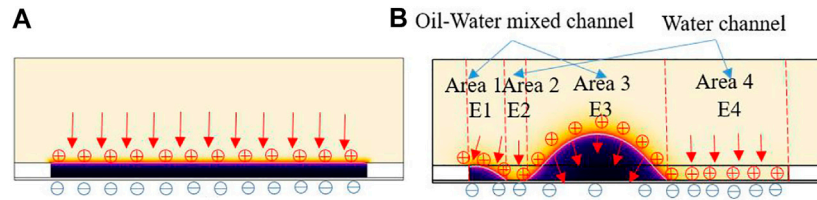


FIGURE 10 | The change of the internal electric field inside of a pixel **(A)** The internal electric field of the initial interface **(B)** The internal electric field in the process of oil movement. E1, E2, E3, and E4 represented the internal electric fields formed by areas 1, 2, 3, and 4, respectively.

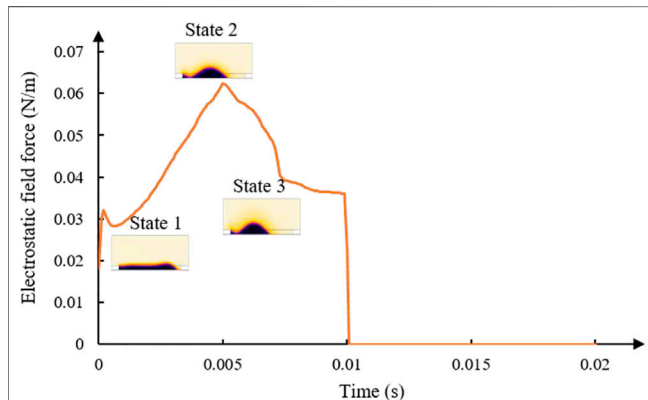


FIGURE 11 | The relationship between fluid status and electrostatic field force. Taking Waveform 2 as the input term, the electrostatic field force in a pixel space was integrated, and the results of the electrostatic field force in the driving period were obtained.

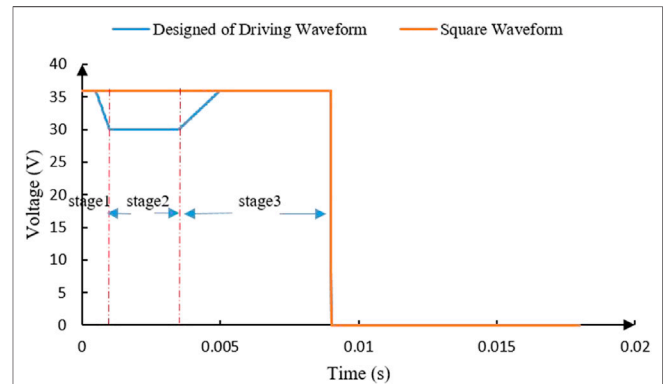


FIGURE 12 | The proposed driving waveform and the traditional square waveform. The proposed driving waveform had three stages which were maintained for 1 ms, 2.5 ms, and 5.5 ms, respectively, and the period of the square waveform and the proposed driving waveform were both 18 ms. The rest of the blue curve overlapped with the square waveform.

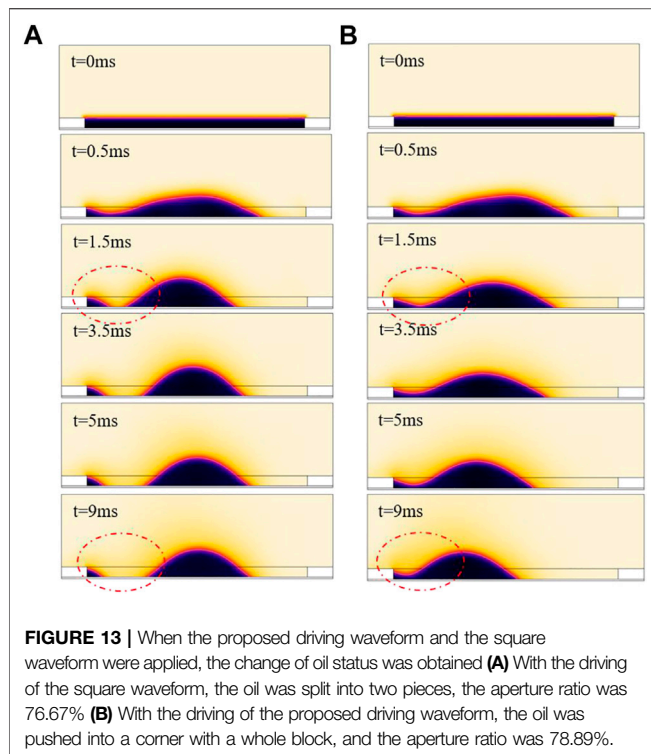
channel. As shown in **Figure 10B**, the internal space of the pixel can be divided into areas 1, 2, 3, and 4, respectively, areas 1, 3 were oil-water mixed channels, and areas 2, 4 were water channels. E1, E2, E3, and E4 represented the internal electric fields formed by areas 1, 2, 3, and 4, respectively. In the analysis process, the water with a high dielectric constant (80) as a conductor of electricity and oil as an insulator was considered. According to **Eq. 24**, the internal voltage U was 0 V in the water channel, so the internal electric field E was 0 (V/m). In the area of the oil-water mixed channel, if U remained unchanged and d was increased, the internal electric field was decreased. On the contrary, the internal electric field was increased. Therefore, the internal electric field force was proportional to the thickness of the oil, and the oil was split easier in the thin area. The red arrows in **Figure 10B** indicated the direction of the internal electric field. When the water was considered as a conductor of electricity, the voltage at the oil-water interface was the same. As the height of the oil increased, the electric field at the high of the oil was smaller, and the electric field at both sides was greater than the highest. Therefore, a non-uniform electric field was formed in the oil, and the oil formed a spherical cap shape with the action of the non-uniform internal electrostatic field.

The change of the internal electrostatic field force inside a pixel was shown in **Figure 11**. The result was obtained by the integral calculation of electrostatic field forces in a pixel space (except the pixel walls). When the oil was in State 1, a new water channel was formed in the oil

ruptured area, and the internal electric field was reduced in this area. So, the electrostatic field force was reduced at this stage. Then, the voltage was increased linearly, the electric field in the pixel space was increased overall. As a result, the electrostatic field force was also increased. When the oil became State 2, the oil was pushed to the highest. Although the voltage kept the maximum, the internal electrostatic field force was reduced. This was mainly due to the larger water channel area.

DRIVING WAVEFORM DESIGN FOR SUPPRESSING OIL-SPLITTING

In a two-dimensional EWD model simulation, a pixel switch-on process can be divided into three stages. In the first stage, oil was ruptured randomly on one side of a pixel. The other side was squeezed down, but not ruptured. This stage was maintained about 1 ms. In the second stage, oil was continuously squeezed, the oil was driven both vertically and horizontally with the action of the non-uniform electrostatic field force. If the voltage was large enough, oil on the side which was not ruptured previously was split. This stage was maintained about 2–5 ms. In the third stage, oil was driven horizontally, and the height of oil was almost unchanged. By analyzing these stages, the conclusions were obtained as follows. The oil was thin and the electrostatic field force applied to the oil was large in the first stage. When a high voltage more than 36 V was



applied, the oil was split into two pieces. The oil-splitting appeared in the first and second stages. So, combined with the analysis of oil movement in the first and second stages, a driving waveform was proposed for suppressing the oil-splitting. The proposed driving waveform was divided into three stages as shown in **Figure 12**. In the first stage, the waveform started at 36 V (high voltage), then was dropped to 30 V rapidly, and maintained for 0.5 ms, respectively. The purpose of this stage was mainly to drive the oil to rupture on one side. In stage 2, the voltage value was maintained at 30 V for 2.5 ms. At this stage, oil was mainly driven in one direction horizontally. In stage 3, when the oil was pushed thick enough, the voltage can be increased, and the oil was not split anymore. This stage was to improve the response speed of the pixel. When the square waveform was applied to this model, the oil was split into two pieces at 1.5 ms as shown in **Figure 13A**, and then the oil was driven to the middle of a pixel at 5 ms. When the proposed driving waveform was applied to this model, the oil was pushed a corner with a whole block as shown in **Figure 13B**. The result showed that the proposed driving waveform can effectively suppress oil-splitting, and the aperture ratio was increased by 2.9% compared to the square waveform.

REFERENCES

- Jones TB. An Electromechanical Interpretation of Electrowetting. *J Micromech Microeng* (2005) 15(6):1184–7. doi:10.1088/0960-1317/15/6/008
- Beni G., and Hackwood S. Electro-wetting Displays. *Appl Phys Lett* (1981) 38(4):207–9. doi:10.1063/1.92322
- Bai PF., Hayes RA., Jin M., Shui L., Yi ZC., Wang L., et al. Review of Paper-Like Display Technologies (Invited Review). *Pier* (2014) 147:95–116. doi:10.2528/PIER13120405

CONCLUSION

In this paper, a two-dimensional EWD model was established. This model was used to simulate the influence of dynamic viscosity, voltage, and waveform on oil-splitting. The oil was easily broken into two pieces with a high voltage. In addition, the internal electrostatic field force and oil movement were affected by each other. On the basis of the traditional square waveform, the proposed narrow falling ramp drove the oil to rupture quickly on one side of a pixel. The proposed low voltage maintenance stage can effectively suppress the oil-splitting. After applying this optimized waveform, the aperture ratio of a pixel was increased. The simulation model can provide a prediction scheme for the selection of oil and the design of the driving system in practical application. By adjusting part of the structure or material parameters of the model, it can be applied to other schemes of EWDs.

DATA AVAILABILITY STATEMENT

The raw data supporting the conclusions of this article will be made available by the authors, without undue reservation.

AUTHOR CONTRIBUTIONS

SL, HS, and QZ: investigation, methodology, formal analysis, editing. SL: writing – review, and editing. All authors contributed to the article and approved the submitted version.

FUNDING

Supported by the National Key Research and Development Program of China (2016YFB0401501), Program for Guangdong Innovative and Entrepreneurial Teams (No. 2019BT02C241), Science and Technology Program of Guangzhou (No. 2019050001), Program for Chang Jiang Scholars and Innovative Research Teams in Universities (No. IRT_17R40), Guangdong Provincial Key Laboratory of Optical Information Materials and Technology (No. 2017B030301007), Guangzhou Key Laboratory of Electronic Paper Displays Materials and Devices (201705030007), and the 111 Project.

- Yi Z., Feng H., Zhou X., and Shui L. Design of an Open Electrowetting on Dielectric Device Based on Printed Circuit Board by Using a Parafilm M. *Front Phys* (2020) 8:193. doi:10.3389/fphy.2020.00193
- Feng H., Yi Z., Yang R., Qin X., Shen S., Zeng W., et al. Designing Splicing Digital Microfluidics Chips Based on Polytetrafluoroethylene Membrane. *Micromachines* (2020) 11(12):1067. doi:10.3390/mi11121067
- Wang L., Yi Z., Jin M., Shui L., and Zhou G. Improvement of Video Playback Performance of Electrophoretic Displays by Optimized Waveforms with Shortened Refresh Time. *Displays* (2017) 49:95–100. doi:10.1016/j.displa.2017.07.007

7. Shen S., Gong Y., Jin M., Yan Z., Xu C., Yi Z., et al. Improving Electrophoretic Particle Motion Control in Electrophoretic Displays by Eliminating the Fringing Effect via Driving Waveform Design. *Micromachines* (2018) 9(4): 143. doi:10.3390/mi9040143
8. Li JS., Tang Y., Li ZT., Li JX., Ding XR., Yu BH., et al. Toward 200 Lumens Per Watt of Quantum-Dot White-Light-Emitting Diodes by Reducing Reabsorption Loss. *ACS Nano* (2021) 15(1):550–62. doi:10.1021/acsnano.0c05735
9. Li Z., Cao K., Cao K., Li J., Tang Y., Ding X., et al. Review of Blue Perovskite Light Emitting Diodes with Optimization Strategies for Perovskite Film and Device Structure. *Opto-Electronic Adv* (2021) 4(2):20001901–15. doi:10.29026/oea.2021.200019
10. Li W., Wang L., Zhang T., Lai S., Liu L., He W., et al. Driving Waveform Design with Rising Gradient and Sawtooth Wave of Electrowetting Displays for Ultra-low Power Consumption. *Micromachines* (2020) 11(2):145. doi:10.3390/mi11020145
11. Yi Z., Huang Z., Lai S., He W., Wang L., Chi F., et al. Driving Waveform Design of Electrowetting Displays Based on an Exponential Function for a Stable Grayscale and a Short Driving Time. *Micromac* (2020) 11(3):313. doi:10.3390/mi11030313
12. Jin M., Shen S., Yi Z., Zhou G., and Shui L. Optofluid-Based Reflective Displays. *Micromac* (2018) 9(4):159. doi:10.3390/mi9040159
13. Yi Z., Shui L., Wang L., Jin M., Hayes RA., and Zhou G. A Novel Driver for Active Matrix Electrowetting Displays. *Displ* (2015) 37:86–93. doi:10.1016/j.displa.2014.09.004
14. Yi Z., Liu L., Wang L., Li W., Shui L., and Zhou G. A Driving System for Fast and Precise Gray-Scale Response Based on Amplitude-Frequency Mixed Modulation in TFT Electrowetting Displays. *Micromac* (2019) 10(11):732. doi:10.3390/mi10110732
15. Liu L., Bai P., Yi Z., and Zhou G. A Separated Reset Waveform Design for Suppressing Oil Backflow in Active Matrix Electrowetting Displays. *Micromac* (2021) 12(5):491. doi:10.3390/mi12050491
16. Hsieh WL., Lin CH., Lo KL., Lee KC., Cheng WY., and Chen KC. 3D Electrohydrodynamic Simulation of Electrowetting Displays. *J Micromech Microeng* (2014) 24(12):125024. doi:10.1088/0960-1317/24/12/125024
17. Walker S. W., and Shapiro B. Modeling the Fluid Dynamics of Electrowetting on Dielectric (EWOD). *J Microelectromech Syst* (2006) 15(4):986–1000. doi:10.1109/JMEMS.2006.878876
18. Zhou M., Zhao Q., Tang B., Groenewold J., Hayes RA., and Zhou G. Simplified Dynamical Model for Optical Response of Electrofluidic Displays. *Displ* (2017) 49:26–34. doi:10.1016/j.displa.2017.05.003
19. Luo Z., Fan J., Xu J., Zhou G., and Liu S. A Novel Driving Scheme for Oil-Splitting Suppression in Electrowetting Display. *Opt Rev* (2020) 27(4):339–45. doi:10.1007/s10043-020-00601-z
20. Roques-Carnes T., Hayes RA., and Schlangen LJM. A Physical Model Describing the Electro-Optic Behavior of Switchable Optical Elements Based on Electrowetting. *J Appl Phys* (2004) 96(11):6267–71. doi:10.1063/1.1810192
21. Yang G., Zhuang L., Bai P., Tang B., Henzen A., and Zhou G. Modeling of Oil/Water Interfacial Dynamics in Three-Dimensional Bistable Electrowetting Display Pixels. *ACS Omega* (2020) 5(10):5326–33. doi:10.1021/acsoomega.9b04352
22. Kim J. Phase-Field Models for Multi-Component Fluid Flows. *Commun Comput Phys* (2012) 12(3):613–61. doi:10.4208/cicp.301110.040811a
23. Zhao Q., Tang B., Dong B., Li H., Zhou R., Guo Y., et al. Electrowetting on Dielectric: Experimental and Model Study of Oil Conductivity on Rupture Voltage. *J Phys D: Appl Phys* (2018) 51(19):195102. doi:10.1088/1361-6463/aabb69
24. Yue P., Feng JJ., Liu C., and Shen J. A Diffuse-Interface Method for Simulating Two-phase Flows of Complex Fluids. *J Fluid Mech* (2004) 515:293–317. doi:10.1017/S0022112004000370
25. Yurkiv V., Yarin AL., and Mashayek F. Modeling of Droplet Impact onto Polarized and Nonpolarized Dielectric Surfaces. *Langmuir* (2018) 34(34): 10169–80. doi:10.1021/acs.langmuir.8b01443
26. Zhu G., Yao J., Zhang L., Sun H., Li A., and Shams B. Investigation of the Dynamic Contact Angle Using a Direct Numerical Simulation Method. *Langmuir* (2016) 32(45):11736–44. doi:10.1021/acs.langmuir.6b02543
27. Cahn JW., and Hilliard JE.. Free Energy of a Nonuniform System. I. Interfacial Free Energy. *J Chem Phys* (1958) 28(2):258–67. doi:10.1063/1.1744102
28. Dolatabadi A., Arzpeyma A., Wood-Adams P., and Bhaseen S. A Coupled Electro-Hydrodynamic Numerical Modeling of Droplet Actuation by Electrowetting. *Colloids Surfa, A Physicoche Eng Aspects* (2008) 323(1/3): 28–35. doi:10.1016/j.colsurfa.2007.12.025
29. Jones TB., Gunji M., Washizu M., and Feldman MJ. Dielectrophoretic Liquid Actuation and Nanodroplet Formation. *J Appl Phys* (2001) 89(2):1441–8. doi:10.1063/1.1332799
30. Jones TB., Fowler JD., Chang YS., and Kim CJ. Frequency-based Relationship of Electrowetting and Dielectrophoretic Liquid Microactuation. *Langmuir* (2003) 19(18):7646–51. doi:10.1021/la0347511
31. Jones TB. On the Relationship of Dielectrophoresis and Electrowetting. *Langmuir* (2002) 18(11):4437–43. doi:10.1021/la025616b
32. Yi Z., Feng W., Wang L., Liu L., Lin Y., He W., et al. Aperture Ratio Improvement by Optimizing the Voltage Slope and Reverse Pulse in the Driving Waveform for Electrowetting Displays. *Micromachines* (2019) 10(12): 862. doi:10.3390/m11012086210.3390/mi10120862
33. Feng HQ., Yi ZC., Sun ZZ., Zeng WJ., Wang L., Yang JJ., et al. A Spliceable Driving System Design for Digital Microfluidics Platform Based on Indium Tin Oxide Substrate. *J Nanoelectronics Optoelectronics* (2020) 15(9):1127–36. doi:10.1166/jno.2020.2838
34. Zeng W., Yi Z., Zhao Y., Zeng W., Ma S., Zhou X., et al. Design of Driving Waveform Based on Overdriving Voltage for Shortening Response Time in Electrowetting Displays. *Front Phys* (2021) 9:642682. doi:10.3389/fphy.2021.642682
35. Kang KH. How Electrostatic fields Change Contact Angle in Electrowetting. *Langmuir* (2002) 18(26):10318–22. doi:10.1021/la0263615
36. Brabcova Z., McHale G., Wells GG., Brown CV., and Newton MI. Electric Field Induced Reversible Spreading of Droplets into Films on Lubricant Impregnated Surfaces. *Appl Phys Lett* (2017) 110(12):121603. doi:10.1063/1.4978859

Conflict of Interest: The authors declare that the research was conducted in the absence of any commercial or financial relationships that could be construed as a potential conflict of interest.

Copyright © 2021 Lai, Zhong and Sun. This is an open-access article distributed under the terms of the Creative Commons Attribution License (CC BY). The use, distribution or reproduction in other forums is permitted, provided the original author(s) and the copyright owner(s) are credited and that the original publication in this journal is cited, in accordance with accepted academic practice. No use, distribution or reproduction is permitted which does not comply with these terms.